ABSTRACT

Title of Thesis: SULFURIZED POLYACRYLONITRILE
SOLID STATE LITHIUM BATTERIES USING
GEL POLYMER INTERLAYERS

Ryan James Moore, Master of Science, 2025

Thesis Directed By: Professor Eric Wachsman, Departments of
Materials Science and Engineering & Chemical
and Biomolecular Engineering

Solid state garnet electrolytes offer stability against lithium dendrite formation, relatively high ionic conductivity, and a wide electrochemical window. They also can block the lithium polysulfide shuttle effect in sulfur batteries. In combination with sulfur cathodes, garnet solid-state electrolytes can increase battery energy densities greatly. In this study, the addition of novel mixed ion electric conductors (MIEC) to solid state batteries is examined. In addition, a poly(vinylidene fluoride)-co-hexafluoropropylene (PVDF-HFP) gel polymer electrolyte is developed and characterized to stabilize the cathode garnet interface. The gel polymer electrolyte had stability up to 4.8V. A lithium conductivity of 5.28×10^{-5} Scm^{-1} and the transference number of 0.103 was calculated. Full cells were constructed with lithium metal and sulfurized polyacrylonitrile. Three different structures were tested. It was found that the addition of MIEC helped create long lasting cells with 80% capacity retention after 303 cycles.

SULFURIZED POLYACRYLONITRILE SOLID STATE LITHIUM BATTERIES USING GEL POLYMER INTERLAYERS

by

Ryan James Moore

Thesis submitted to the Faculty of the Graduate School of the
University of Maryland, College Park, in partial fulfillment
of the requirements for the degree of
Master of Science
2025

Advisory Committee:
  Professor Eric Wachsman, Chair
  Professor Paul Albertus
  Professor Chunsheng Wang

Acknowledgements

I would like to thank my advisor, Dr. Wachsman, for the support during my time at UMD. I would like to thank Dr. Albertus and Dr. Wang for being on my committee.

I would like to thank the Battery 500 consortium for the financial support for this project.

I would like to thank the members of the battery 500 project team in the Wachsman lab and the rest of the lab members for the support, collaboration, and help during my time at UMD.

Thank you to my family for your support and believing in me.

Table of Contents

List of Tables

List of Figures

List of Abbreviations

Materials

BBP	Butyl Benzyl Phthalate
DME	1,2-Dimethoxyethane
DOL	1,3-Dioxolane
HDPE	high density polyethylene
LiFSI	Lithium bis(fluorosulfonyl)imide
LiTFSI	Lithiumbis(trifluoromethanesulfonyl)imide
LLZO	Lithium Lanthanum Zirconium Oxide
LLZTO	Lithium Lanthanum Zirconium Tantalum Oxide
MIEC	Mixed Ion-Electron Conductor
PAG	Polyalkylene Glycol
PMMA	Poly(methyl methacrylate)
PVB	Polyvinyl Butyral
PVDF-HFP	Poly(vinylidene fluoride-co-hexafluoropropylene)
SPAN	Sulfurized Polyacrylonitrile

Methods

EIS	Electrochemical Impedance Spectroscopy
SEM	Scanning Electron Microscopy
XRD	X-Ray Diffraction

Chapter 1: Introduction

As global temperatures increase, there has been an emphasis on finding ways to decarbonize the global economy. In 2018, transport accounted for 24% of global CO_2 emissions.[1] Road vehicles made up 45% of transport emissions.[1] There are real opportunities to greatly reduce the carbon footprint of those vehicles with the development of electric vehicles (EVs). This need for electric vehicles has caused demand for batteries to significantly increase. According to Degen et. al. the demand for energy from lithium ion battery and post lithium-ion batteries is forecasted to increase fivefold from 2025 to 2040.[2] The demand for more batteries leads to demand for the better batteries. With increases in energy density, there could be cost savings in the transport and manufacturing of batteries allowing for batteries at greater scale.

A major goal in developing better batteries in the use of the lithium metal anode. Lithium metal has an extremely high specific capacity of 3860 mA h g^{-1}.[3] However, the anode develops dendrites which can lead to cell failure.[3] Solid state separators, such as lithium lanthanum zirconium oxide (LLZO) have been developed as a way to prevent lithium dendrites and to be chemically compatible with the anode.[4] Recently, Alexander et. al. developed a material to further improve the lithium plating and stripping of lithium around solid state separators.[5]

Further room for improvement can be found with sulfur based cathodes which have a high specific capacity of 1675 mAh/g.[6] However, the interface between LLZO and sulfur has to be stabilized.[7] The goal of this study is to examine the effects of the novel battery material MIEC on quasi solid-state batteries. A further goal from this study is to develop a suitable gel polymer electrolyte (GPE) for quasi solid-state batteries to pacify the interface between sulfur-based cells and garnet solid-state electrolytes.

Chapter 2: Literature Review

Section 2.1 Literature Review

2.1.1 Battery Technology

Batteries are devices that store chemical energy and release that energy as electricity. Allesandro Volta is credited with inventing the first battery with the volta pile in 1800.[8] The pile consisted of zinc and copper disks stacked on top of each other separated by brine soaked cloth.[8] Since then, significant developments have been made to further the energy density and performance characteristics of batteries. This includes the invention of the lead acid battery in 1859, which is still used in cars today.[8] One of the most recent and impactful developments has been the invention of lithium-ion batteries. John B Goodenough, M. Stanley Whittingham, and Akira Yoshino received the 2019 Nobel prize in chemistry for this work.[9] Lithium-ion batteries use intercalation materials, such as graphite and lithium cobalt oxide (LCO) that allow lithium ions to shuttle back and forth between layered structures allowing for high cycle life and high energy density. Currently, demand for higher energy density batteries continues to drive further development.

Lithium metal is a nearly perfect candidate for high energy batteries. It has an extremely high specific capacity of 3860 mA h g^{-1} compared to graphite's 372 mA h g^{-1}.[3,10] It also has the lowest voltage against the standard hydrogen electrode at −3.040 V.[3] The issues associated with using lithium metal are poor coulombic efficiency and dendritic growth.[3] The dendrites can lead to cell failure when the dendrites puncture the separator creating a short circuit. Most approaches towards managing the dendrite formation has come from engineering the solid electrolyte interphase (SEI) to resist forming lithium dendrites by engineering the components of the liquid electrolyte.[3] These methods improve the cycle life of lithium metal cells, but are not fully successful at hindering dendrite formation. The alternative to using a liquid electrolyte is to use a solid separator. Solid separators with high shear moduli can suppress dendrite formation.[11] In addition, solid separators can eliminate crosstalk between anode and cathode, allowing for optimization of each electrode to take place independently. They can eliminate crosstalk because solid state electrolytes have different lithium-ion conduction mechanisms than liquid cells. Liquid cells rely on a liquid electrolyte with lithium-ions dissolved in it. The ions move through diffusion across a concentration gradient. In a solid electrolyte, lithium ions can hop across vacancies in the crystal structure, while other larger ions are blocked from moving within the structure. With these advantages, solid state separators look to give high cycle life over conventional liquid cells.

2.1.2 Garnet Solid Electrolyte

There are multiple design factors when it comes to choosing a solid separator for lithium metal batteries. Chemical stability against lithium metal and cathode materials is required.[6] A electrochemical window, ionic conductivity, and mechanical properties should also be considered.[4] Solid separators can be split into inorganic and organic compounds. Organic compounds are typically solid polymer membranes or gel polymer electrolytes. Polymer separators generally exhibit a trade-off between mechanical properties and good ionic conductivity.[4] Among inorganic solid state separators, sulfide based, Argyrodite, Perovskite, and Garnet separators have been considered.[12] Each of these have design trade-offs, for example, sulfide based inorganic separators have good ionic conductivity. However, they are watersensitive and must be handled in an inert atmosphere, making processing difficult.[4] This review will further discuss garnet solid separators due to their exciting properties.

Garnet solid separators meet many of the design criteria. They are stable against lithium metal, have a large electrochemical window, and have high ionic conductivity.[4] These lithium ion conducting oxides are derived from the ideal orthosilicate garnet structure of $A_3B_2(XO_4)_3$.[12] The equivalent of this in a lithium containing structure would be $Li_3La_3Te_2O_{12}$.[4] However, this compound has poor lithium conductivity. To increase the lithium conductivity, higher lithium content is needed.[12] In addition, having the cubic structure of lithium lanthanum zirconium oxide (LLZO) is critical to maintain high ionic conductivities.[12] Efforts to increase lithium content led "lithium stuffed" garnets. In 2007, Weppner et al. first reported high ionic conductivity garnet ($Li_7La_3Zr_2O_{12}$) with up to $3x10^{-4}$ Scm^{-1} at room temperature.[13] However, the reported structure was only cubic due to possible alumina contamination during high temperature processing.[14] Subsequent studies have found that doping LLZO with Ta, to form Lithium Lanthanum Zirconium Tantalum Oxide (LLZTO), leads to a stable cubic structure and high ionic conductivity.[15] Despite their benefits, garnet solid separators do have issues. Controlling the interface between the electrodes and the separator is a large problem. Often, stack pressure is required to maintain contact between the electrode and the separator. Applying stack pressure is often infeasible in devices such as mobile phones due to space and cost constraints. Also, Garnet is brittle, which can lead to cell failure if not handled properly.

2.1.3 Sulfur Cathodes

Sulfur, as cathode material, has gained a lot of attention recently. Sulfur has a high theoretical specific capacity (1675 mAh g^{-1}).[6] The material is abundant and can be sourced at a low cost.[6] However, sulfur cathodes come with unique challenges. Sulfur an insulator by nature, which limits its kinetics in electrochemical reactions.[6] Sulfur is a conversion cathode material with many intermediate products known as lithium polysulfides. The lithium polysulfides are soluble in electrolyte and can migrate towards the anode and react with the anode causing loss of capacity. This is known as the polysulfide shuttle effect.[6] The cathode also undergoes large volume changes during cycling, which causes a lot of mechanical stress.[6] Traditional methods to solve these challenges involve the addition of carbon to provide electronic conductivity.[6] The addition of lithium nitrate in the electrolyte can protect the anode against the polysulfide shuttle effect.[16] However, lithium nitrate is progressively consumed during cycling leading to limited cycle life.[16] The addition of high amounts of carbon also limits energy density. Further development of potential remedies to sulfur's challenges led to the development of sulfurized polyacrylonitrile (SPAN).[17]

2.1.4 Sulfurized Polyacrylonitrile

SPAN is conductive polymer network where sulfur is connected to the network through S-N and S-C covalent bonds.[18] The polymer network is comprised of conjugated pyridine rings that host sulfur. The carbon network gives SPAN several advantages. Since sulfur is molecularly dispersed within the chain, sulfur utilization is very high compared to typical carbon-sulfur composites.[19] SPAN also has better electronic conductivity[19], requires less liquid electrolyte[20], and undergoes lower volumetric changes than sulfur cathodes.[21] SPAN was first prepared by Wang et. al.[17] by heating polyacrylonitrile (PAN) and sulfur at 300°C under argon. Subsequently, extensive research has gone into improving the preparation of SPAN to improve sulfur content and cycle life. The ratio of PAN to Sulfur, heating temperature, vapor pressure, and molecular weight of PAN all affect the performance of characteristics of SPAN.[22]

2.1.5 Gel Polymer Electrolytes

Gel Polymer Electrolytes (GPE) are formed by incorporating an organic liquid electrolyte into a polymer matrix. The liquid electrolyte acts as a plasticizer and allows free movement of the polymer chains allowing for high ionic conductivity. GPEs can combine the high ionic conductivity of liquid electrolytes with the mechanical properties of solid polymer electrolytes.[22] The choice of polymer used in the electrolyte depends on the polymer's crystallinity.[22] The addition of inorganic fillers and lithium salts can enhance the ionic conductivity of the polymer membrane.[22] A common method of creating GPEs is called solution casting.[23] It is commonly used because of its simplicity and lack of required sophisticated equipment. The polymer and salt are dissolved in a solvent and mixed. The mixture is then cast onto a substrate and dried at low temperature. The low temperature drying restricts the movement of polymer chains resulting in a less crystalline matrix.[23] The electrolyte is then introduced by soaking the polymer matrix in the electrolyte.

Section 2.2 Previous Works

2.2.1 Garnet Tape Cast Structures

The Wachsman group has made large contributions to lowering the resistance of garnet batteries through the development of 3D tape cast structures. Typical garnet separators were thick polished pellets (100–150 μm).[24] However, the use of tape casting, a processing technique where a doctor blade spreads a ceramic slurry onto a carrier substrate, allows the creation of thin dense (10-20 μm) separators that dramatically lower the area squared resistance (ASR).[24] The dense separator is supported by a porous layer in into which lithium can be melted. The high surface area of the porous layer allows for uniform stripping and plating of lithium metal during cycling. The lithium metal is able to wet the garnet through the use of atomic layer deposition technology (ALD).[25] This allows for a very low interfacial resistance compared to previous techniques. In addition to the low interfacial resistance, zero stack pressure is required to maintain contact between the anode and separator. The 3D structure is also highly tunable and can be laminated with other tapes to create multi-tiered structures. Bilayer structures are used when a dense layer is stacked on top of a porous layer. A symmetric design can be used where a dense layer is surrounded on both sides by a porous layer. This is called a trilayer.

The newest development from the Wachsman lab is the use of mixed ion-electric conductors (MIEC) in the porous layer.[5] While garnet electrolytes have low electronic conductivity, MIEC has additional electronic conductivity to help with lithium plating. The result of this development allows symmetric lithium cells to be cycled at 60 mA cm^{-2}.[5]

2.2.2 Sulfur development

Wachsman and Hu group have collaborated significantly on solid state sulfur-based batteries and gel polymer electrolytes. Fu et. al.[26] studied the interfacial stability of sulfur and its reaction products against the garnet solid electrolyte. The study found that LLZO is suitable for sulfur cathodes. During cycling, a 5 nm thick interphase layer that contains Li_2S and Li_2SO_4 forms on the surface of the garnet. The interphase layer protects the garnet from further reactions. The garnet solid separator also blocks the polysulfide shuttle effect which leads to capacity loss in sulfur cells.

Further development has gone into Li-S cells with garnet separators. Shi et. al. incorporated a polyethylene oxide (PEO) based interlayer to stabilize the garnet sulfur interface.[7] When using a high sulfur loading cathode in contact with LLZTO bilayers, Shi observed overcharging behavior. The behavior is characterized by an indefinite charging phase during cycling and sudden voltage fluctuations. See figure 1 below for an example of catastrophic overcharging. Lanthanum segregation on the surface of the garnet was attributed to the cause of the cell failure. However, it is not possible to lower the La amount in garnet without suffering major ionic conductivity penalties. Therefore, a polymer interlayer was incorporated to protect the bilayer. The polymer interlayer additionally provides support for the large volumetric changes sulfur undergoes during cycling.

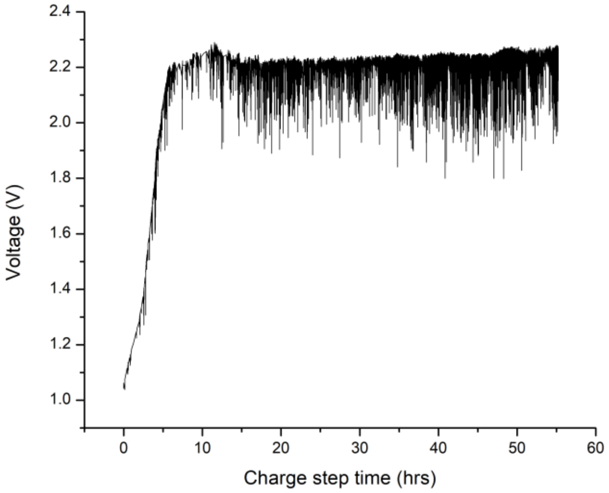

Figure 1: Example of overcharge in Li-S cells. SPAN in contact with garnet separator. Charge rate of C/20 was chosen. The cell was unable to reach 2.8V target even after 60hrs of charging.

Following stabilizing the interface, development was done to optimize the polymer interlayer. Previously, large amounts of catholyte (20 µL cm^{-2}) were required to wet the thick polymer interlayer.[27] Shi et. al. utilized SPAN, which requires less electrolyte than sulfur, and a novel interlayer consisting of polymerized 1,3-dioxolane. (PDOL).[27] 1,3-Dioxolane (DOL) was polymerized in-situ through the addition of Lithium bis(fluorosulfonyl)imide (LIFSI) on top of the garnet dense layer providing excellent contact. The PDOL interlayer was extremely thin (3µm). The PDOL layer was turned into a GPE by adding 1M LIFSI in 1,2-Dimethoxyethane

(DME). The result was a SPAN cell with excellent specific capacity and capacity retention. The capacity retention was 80% over 265 cycles at 0.2C. The GPE ionic conductivity was measured at 4.5 mS cm^{-1}.[27]

2.2.3 PVDF-HFP membranes

Polyvinylidene fluoride (PVDF) polymers are a good choice for polymer solid separators. The polymer has good mechanical strength, excellent thermal stability, a high dielectric constant, chemical stability, and a wide electrochemical window.[28] The polymer has limited ionic conductivity because of its crystallinity. To lower the crystallinity, PVDF is copolymerized with hexafluoropropylene (HFP) to form poly(vinylidene fluoride-co-hexafluoropropylene) (PVDF-HFP). The lower conductivity allows PVDF-HFP to have better liquid holdup and increase ionic conductivity when compared to PVDF.

Section 2.3 Characterization Methods

2.3.1 Electrochemical Testing

Electrochemical impedance spectroscopy (EIS) is a technique to measure the impedance of materials and electrochemical cells. EIS works by applying AC potential to a cell. The AC current response is then recorded.[29] The response can be interpreted through sinusoidal functions. The functions can be represented mathematically by having an imaginary and real portion of the response. This is visually represented in Nyquist plots. To apply physical meaning to the data it can be modelled with equivalent electrical circuits.

While LLZTO is a single ion conductor, GPEs are not. Therefore, lithium conductivity must be separated from the ionic conductivity to make comparisons. The transference number is used to determine the lithium conductivity from the ionic conductivity. The transference number is the fraction of current carried by an ionic species. The Bruce-Vincent method is commonly used to measure the transference number in GPEs.[30] The method uses the polarization of a lithium symmetric cell and the GPE between two electrodes. Polarization creates a concentration gradient of charged species within the GPE. The spike in current measured and the subsequent relaxation of current to a steady state value can be used to calculate the transference number. To account for electrode effects, EIS measures the interfacial resistance of the before and after the use of polarization. The method assumes a low step voltage is applied (<10mV) and the electrolyte is dilute.[30]

The electrochemical performance of the cell is evaluated with cell cycling. The cell is repeatedly charged and discharged, usually at a given current, to a specific voltage.[31] The C-rate can be used to discuss how fast the cell was charged or discharged. It is a measure of the cell's capacity relative to the rate at which it can be fully charged or discharged.[31] At a rate of 1C, the cell will be charged in 1 hour. At a rate of 0.5C the cell will be charged in 2 hours. The coulombic efficiency is the measure of how efficient the cell is.[31] The coulombic efficiency is the cells discharge capacity divided by the charge capacity.

2.3.2 Scanning Electron Microscopy (SEM)

SEM is a technique to take high resolution and high magnification images.[30] The microscope is able to take high magnification images because electrons have a much smaller wavelength than light.[32] The microscope uses an electron source to emit electrons and direct them towards the sample. The electrons interact with the sample and the sample emits secondary electrons, which can be detected by a detector.[32] Much like an optical microscope, the electron microscope uses lenses to focus and direct the beam to improve the clarity of the images generated. The high magnification images are very useful for studying structures and features than are on the micron or smaller scale.

Chapter 3: Methodology

<u>Section 3.1 Introduction</u>

Previous work using SPAN and garnet only used LLZTO. The development of MIEC allows for enhanced cycling ability of solid-state cells. MIEC bilayers and trilayers were synthesized to see the improvement of the material on SPAN batteries. LLZTO bilayers were produced to make a comparison between the two different materials. Additionally, the use of gel polymer electrolytes stabilizes the interface between SPAN and garnet. PVDF-HFP interlayers with LiFSI were developed to protect the cathode side of the garnet separator. The GPE was wet with 1M Lithium bis(trifluoromethanesulfonyl)imide (LiTFSI) in 1:1 DOL/DME. The GPE was characterized by EIS, LSV, and DC polarization. Cells with SPAN were constructed and cycled to assess the electrochemical performance.

<u>Section 3.2 Experimental</u>

3.2.1 Materials

To produce PVDF-HFP polymer membranes, PVDF-HFP pellets were obtained from Sigma Aldrich. N,N-Dimethylformamide (DMF) (anhydrous, 99.8%) was obtained from Sigma Aldrich. LIFSI (99.9%) was obtained from Alfa Chemistry.

To produce LLZTO and MIEC solid tapes, Lithium Hydroxide Monohydrate ($LIOH\cdot H_20$, ≥98%) was obtained from Sigma Aldrich. Zirconium oxide (ZrO_2) was obtained from Inframat Advanced Materials. Lanthanum Oxide (La_2O_3) was obtained from GFS Chemicals. Tantalum Oxide (Ta_2O_5) and Cerium Oxide (CeO2, 99.99%) were obtained from Alfa Aesar. Praseodymium Oxide (Pr_6O_{11}) was obtained from Sigma Aldrich. Poly(methyl methacrylate)

(PMMA) Spheres (MX-150 1.5μm and MX-1500H 15μm) were obtained from Soken-Kowa Chemical. Menhaden fish oil, Butyl Benzyl Phthalate (BBP), Polyalkylene Glycol (PAG), Polyvinyl Butyral (PVB) were all obtained from Tape Casting Specialists. Ethanol (200 proof, anhydrous) and Isopropyl alcohol (IPA, 99.5%+) were obtained from Pharmco.

To produce SPAN, elemental sulfur and polyacrylonitrile (PAN, Mw. ~151 000) were obtained from Sigma Aldrich.

To produce coin cells, stainless steel CR2032 coin cells were obtained from MTI Corp. Lithium metal foil (99.9%) was obtained from MTI. LiTFSI was obtained from Sigma Aldrich. DME (anhydrous 99.5%) and DOL (anhydrous 99.8%) were obtained from Sigma Aldrich.

3.2.3 Preparation of Garnet Bilayers and Trilayers

Powders for the tapes were prepared from precursors. The target composition for MIEC was $Li_{6.4}Ga_{0.2}Pr_3Zr_{1.8}Ce_{0.2}O_{12}$ and for LLZTO, it was $Li_{6.75}La_3Zr_{1.75}Ta_{0.25}O_{12}$. The precursors for LLZTO were $LIOH \cdot H_20$, La_2O_3, ZrO_2, and Ta_2O_5. Prior to use, the La_2O_3 was calcined at 950°C to remove carbonates. The precursors for MIEC were $LIOH \cdot H_20$, Ga_2O_3, Pr_6O_{11}, ZrO_2, and CeO_2. The precursors for LLZTO and MIEC were weighed out using a Metler Toledo micro balance. For the LLZTO powder 10% excess LIOH·H20 was added to account for lithium loss. For MIEC powder this was 30% excess. The precursors for each composition were placed in high density polyethylene (HDPE) mill bottles containing 5mm and 10mm yttria-stabilized zirconia (YSZ) milling media for mixing. The precursors were milled for 3 days in IPA and then dried in an oven overnight at 100°C. The powders were collected and then grinded by hand with a pestle and mortar. The precursors powders were both calcined at 900°C for 10 hours with up and down ramp rates of 3°C/min. The calcined powders were milled for size reduction. For LLZTO powders being used in dense tape, the powder was milled down to 500nm particle size using 5mm and 10mm in IPA. The powder was dried and then further milled down to 300nm using 2mm and 5mm milling media. For LLZTO and MIEC powders being used in porous tapes, the powders were milled down to 500nm using 5mm and 10mm milling media in IPA. Particle size was verified using a Malvern Zetasizer that uses dynamic light scattering.

The powders were then prepared to make tapes. A tape slurry was prepared by mixing the powder with ethanol and fish oil in a bottle with 5mm and 10mm milling media. After one day of milling, PVB, BBP, and PAG were added. The slurry was milled for another day. For dense tapes, the slurry was degassed in a Thinky Mixer at 1500RPM until the desired viscosity was reached and then tape cast at 152µm onto Mylar. For porous tapes one hour before degassing, PMMA spheres of 15µm and 1.5µm particle size were added in equal amounts. The slurry was then degassed and then tape cast at 254 µm on to Mylar.

The tapes were then prepared to be used as a solid separator. The tapes were laminated to form bilayers and trilayers. A bilayer is made first by laminating two 7cm x 4cm pieces of dense tape together using a hot press at 2 MT of pressure for 5 minutes. Then on one side a piece of porous tape is laminated to the dense laminated tapes. To make a trilayer, the same procedure is followed and then another porous tape is laminated onto the opposite side of the laminated porous tape, giving the porous-dense-porous structure. The tapes are then sintered at 1050°C for 3 hours under O_2 flow. A sintering temperature of 1100°C was not used because of MIEC pore collapse. The laminated tape was placed between two layers of sacrificial tape to provide a uniform lithium source to account for lithium loss during sintering. The tapes were sintered on a MgO plate in a tube furnace.

The sintered tape was then collected and brushed to remove any excess sacrificial tape. The sample was then laser cut using a Muse Full Spectrum laser into 1cm x 1cm squares. The samples were subsequently placed in a tube furnace and heated to 850°C under Ar flow for carbonate removal. The samples were transferred to Forge Nano ALD chamber. The samples underwent 20 cycles of ZnO ALD.

3.2.4 Preparation of SPAN

Elemental sulfur and PAN were mixed in a milling bottle with a mass ratio of 8:1. The mixture was mixed overnight on a ball mill in IPA. The mixture was then dried using a Shlenk line. The mixture was then heated to 300°C at a heating rate of 5°C/min. The sample was held at temperature for 7.5 hours while flowing argon. The mixture was then cooled to room temperature. The mixture was analyzed by a LECO elemental analyzer by Nora Hamovit. The SPAN powder was found to be 37% sulfur content. See appendix section A.1 for sulfur content calculation.

3.2.5 Preparation of PVDF-HFP Interlayers

PVDF-HFP was dissolved in DMF solvent at a ratio of 0.2g/mL. Then LIFSI salt was added to the solution at a mass ratio of 7:3 PVDF-HFP to LIFSI. The solution was mixed with magnetic stirring overnight at 40°C. The mixture was syringed onto the middle of a coin cell top cover (~0.02-0.03g). The syringe tip was used to remove any bubbles formed during transfer. The interlayer was dried overnight at on a hotplate at 40°C. The interlayers were manually peeled off the stainless-steel support.

The liquid uptake of the PVDF-HFP interlayer was measured by weighing the dry interlayer first. The interlayer was soaked in 1M LiTFSI in 1:1 DOL/DME. The calculation is done by following equation (1) below, where $W$is the final weight and W_0 is the initial weight.

$$Liquid\ Uptake = \frac{W - W_0}{W_0} \tag{1}$$

During liquid uptake the GPE swells. The thickness will increase. The thickness is difficult to measure with a micrometer after swelling without compressing out the liquid. Since thickness is important to measuring the conductivity of the GPE, the following equation (2) was used to estimate the thickness after swelling. Where l_{dry} is the initial thickness of the polymer. l_{gel} is the thickness after swelling. V_{liq} is the volume of the electrolyte. A is the area of the polymer interlayer.

$$l_{gel} = \frac{l_{dry}A - V_{liq}}{A} \tag{2}$$

3.2.6 Preparation of cells

All cell preparation took place in a glovebox with argon atmosphere. The O2 and H2O content were both measured at 0.1 PPM. Following ALD, the bilayers were placed on a hot plate and heated to 265°C. Lithium metal strips were cut and placed on SS spacers. Once melted the lithium was spread and cleaned with a razor blade. The bilayer with the porous layer facing downward was placed on top of the lithium and the lithium wet the porous layer immediately.

A cathode slurry of SPAN was prepared. The slurry consisting of 8:2 weight ratio SPAN to graphene nano wire was mixed in NMP overnight using magnetic stirring. Cathodes were prepared by drop casting the slurry on top of a carbon felt current collector. The cathode was dried at 165°C for 1 hour on a hot plate under inert atmosphere.

Cells were assembled by placing the polymer interlayer on top of the bilayer and then wetting the GPE with 10μL of 1M LiTFSI in 1:1 DOL/DME. The DOL/DME was dried using 4 Å molecular sieves prior to use. The cathode was then placed in contact with the interlayer. The coin cells were crimped by using an MTI coin cell crimper at 500 PSI of force. The MIEC trilayer cell was prepared by George Alexander.

3.2.7 Electrochemical Characterization.

All electrochemical characterization occurred at room temperature. A multichannel Arbin was used to cycle the cells. Cells were held at a 6hr rest step before cycling. After rest, one formation cycle for the cells took place at C/20 constant current charge and discharge. The cells were cycled at a 1-2.7V voltage range. Cycling of cells was at a C/4 constant current rate, with a 2.7V constant voltage charge step after the constant current charge step.

DC polarization was done by assembling a PVDF-HFP interlayer coin cell between two lithium electrodes. A step voltage of 10mV was applied and the test lasted for 6hrs. EIS measurements of the lithium symmetric cells were done before and after polarization.

EIS was conducted to measure the bulk resistance of the GPE. Coin cells with PVDF-HFP interlayers between two stainless steel electrodes were used. PEIS was done with an amplitude of 10mV applied. The scan took place between 1HZ to 1MHz.

For linear sweep voltammetry, coin cells were assembled with PVDF-HFP interlayers, with a lithium metal strip as one electrode and stainless steel as the other. A sweep rate of 5 mV/s was used. The sweep went from 2V to 7V vs ref. A second cell was prepared to test the reduction potential. The sweep went from 2V to -2V vs ref. DC polarization, LSV, and EIS were conducted on a multichannel Biologic.

From the lithium symmetric cell polarization test and EIS measurements, the data can be used in equation (3) below to find the transference number. Where t_{Li^+} is the transference number, ΔV is the potential difference, I_0 is the initial current, I_{SS} is the steady state current, $R_{p,0}$, is the initial interfacial resistance, and $R_{p,SS}$ is the steady state interfacial resistance.

$$t_{Li^+} = \frac{I_{ss}\left(\Delta V - I_0 R_{p,0}\right)}{I_0\left(\Delta V - I_{SS} R_{p,SS}\right)} \tag{3}$$

The results of the EIS with stainless steel electrodes and GPE separator can give the bulk resistance value, which is used in equation (4) below to find the ionic conductivity. Where σ_t is the ionic conductivity, l is the thickness, A is the area, and R is the bulk resistance. Given equations (3) and (4), lithium conductivity (σ_{Li^+}) can be found using equation (5).

$$\sigma_t = \frac{l}{RA} \tag{3}$$

$$\sigma_{Li^+} = t_{Li^+} \times \sigma_t \tag{4}$$

Chapter 4: Results and Discussion

4.1 Results

4.1.1 Development of MIEC bilayers and trilayers

The preparation of MIEC bilayers and trilayers required some changes to the SOP that is usually used for LLZTO bilayers and trilayers. The first issue encountered was pore collapse. See figure 2 below for an example of pore collapse. Pore collapse is when the porous layer is unable to support itself and then sinters into the dense layer. This results in an overly thick dense layer as well as the porous network not forming. Lack of a porous network would interrupt the lithium wetting process and result in cells with high impedance. The pore collapse can be attributed to MIEC's different sintering behavior.

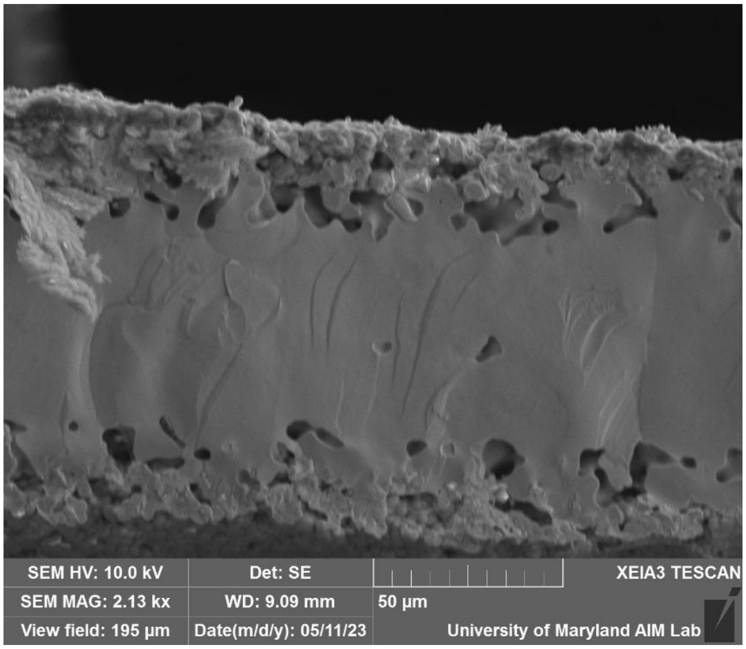

Figure 2: MIEC trilayer sintered at 1100°C for 3 hrs. Signs of the pores collapsing into the dense layer. The pores cannot be lithium infiltrated.

The issue was resolved by lowering the sintering temperature from 1100°C to 1050°C for 3 hours. See below figure for an example of a MIEC bilayer without pore collapse. However, lowering the sintering temperature can result in more difficulties in forming a fully dense defect-free dense layer. Lithium dendrite can propagate in voids and grain boundries leading to short circuits.[33] The samples were found to be dense enough to be usable in cycling, but future efforts may be directed towards lowering the amount of defects in the dense layer.

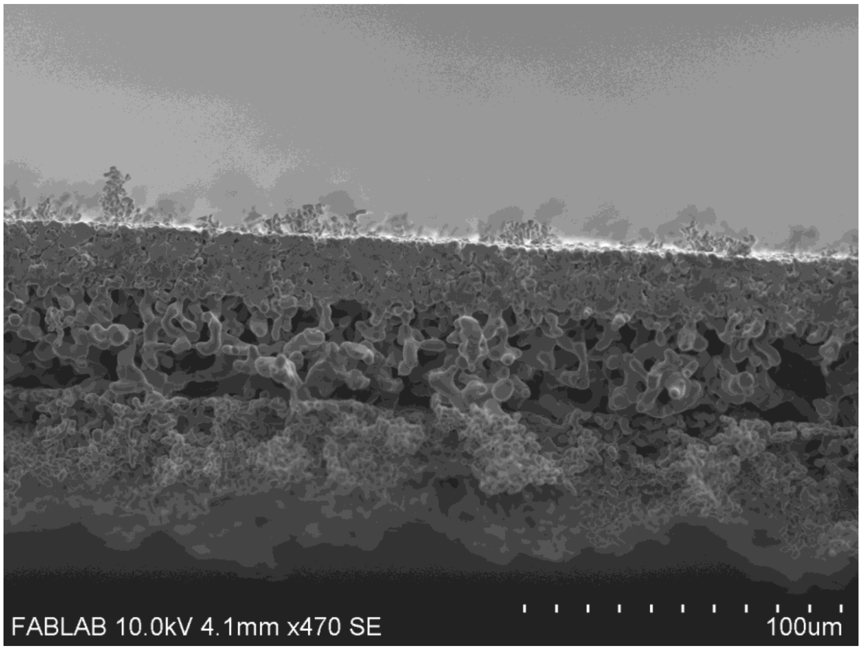

Figure 3: MIEC bilayer sintered at 1050°C for 3hrs. Visible voids forming in the dense layer. Adequate porosity. The bottom layer is the sacrificial tape still attached, which can be removed through brushing.

The second issue encountered was the sacrificial tape sintering to the porous layer. The sacrificial tape is a tape composed of the precursor materials of LLZTO. The tape provides a uniform source of lithium to make up for lithium loss during sintering and is placed on both sides of the sample during sintering. The sacrificial tape under normal circumstances does not sinter to the sample and can be removed with a brush. The stress applied from the shrinkage of the sacrificial tape also warped the sample. The issue was because of MIEC's behavior under tape casting. The tapes created by MIEC are much tackier than LLZTO. The tackiness is a property that is given by the binder in the green tape. To remedy the situation, sacrificial tapes with 30% less binder and plasticizer were used to lower the tackiness and allow the tape to easily be removed from the sample after sintering. See figure 3 below for a sample with the sacrificial tape sintering to the sample and without.

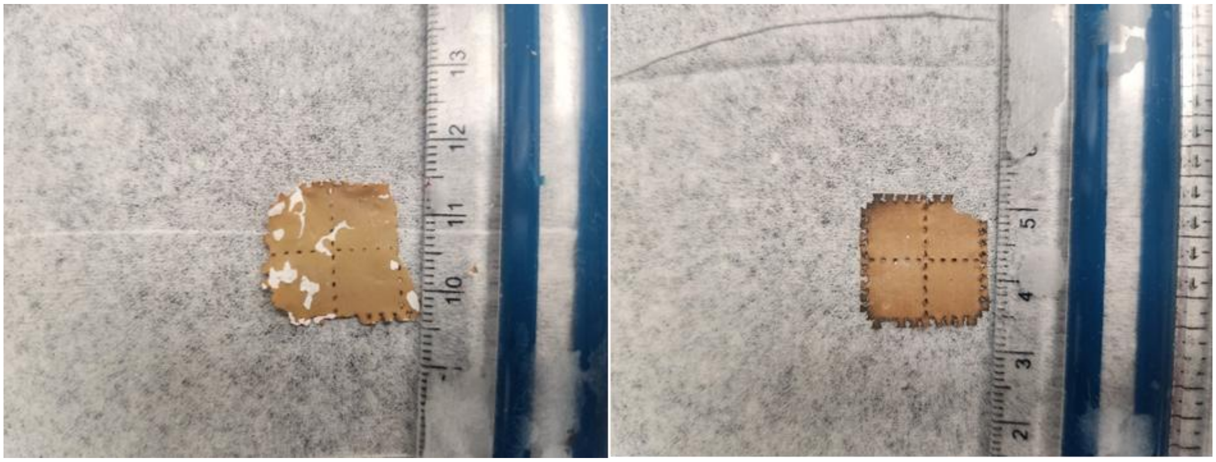

Figure 4: Left: sintered MIEC bilayer with sacrificial tape sintering to porous layer. Right: MIEC bilayer without sacrificial tape sintering to porous layer.

4.1.2 PVDF-HFP Interlayer Characteristics

Following the preparation of the PVDF-HFP interlayers, characterization was done. The interlayers thickness was measured before electrolyte wetting using a digital micrometer. The interlayer was placed between two stainless steel spacers to flatten the interlayer to make measurement easier. The thickness was also verified with SEM, see below in figure 4. The thickness of the interlayers was 40-100μm depending on the amount of solution left to dry. Any thickness lower than 40μm was unable to be peeled off the support because of the lack of mechanical strength. The area of the GPEs were found by taking images with a camera and analyzing the image with ImageJ.

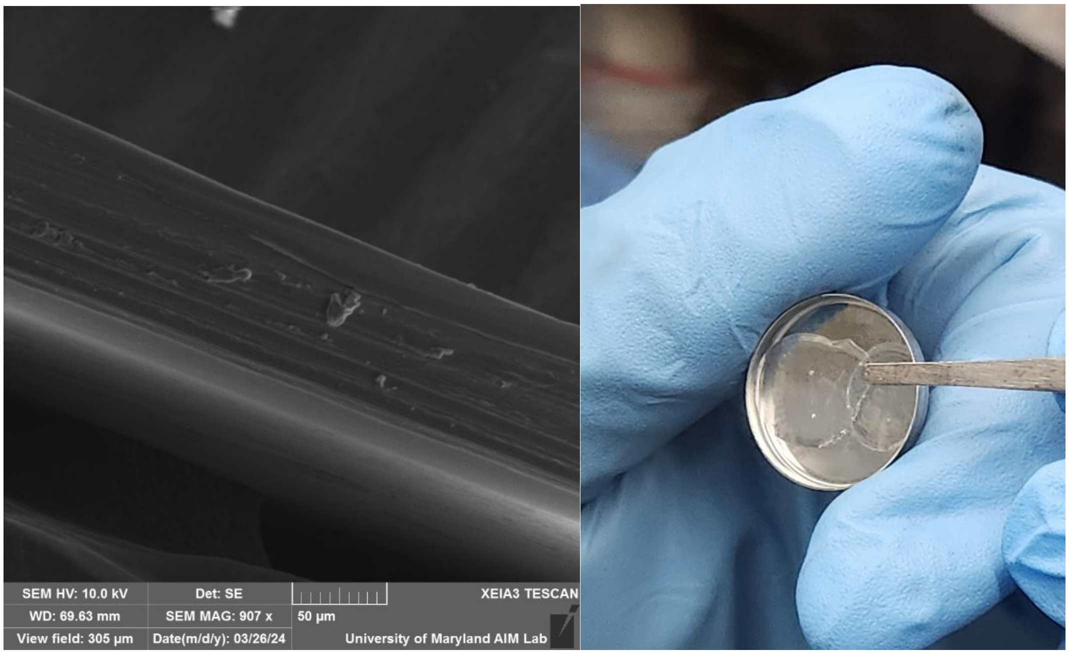

Figure 5:Left: SEM of dry PVDF-HFP interlayer membrane 80μm thick. Right: image of cast PVDF-HFP interlayer. Forms a freestanding interlayer.

The liquid uptake is a good measure to understand how much liquid the interlayer can absorb. Since the electrolyte acts as plasticizer, the amount of liquid absorbed is directly correlated to the ionic conductivity. The liquid uptake was measured to be 201%. The weight added in the liquid uptake test is equivalent to 10μL, which is the same amount added to the cells that were constructed for cell cycling. However, if the membrane was only dipped into the electrolyte and not soaked in electrolyte, the liquid uptake is 36%. Therefore, it is important to note in which way electrolyte was added to the interlayer for testing.

Linear sweep voltammetry allows us to find the oxidation potential. The oxidation and reduction potential is where a reaction between the GPE and lithium occurs indicating operating the cell at that voltage will cause damage to the cell's performance. The results are plotted in figure 5 below. The exact reduction potential can be extrapolated from the curve. To find it, a line was fitted to the linear part of the curve (5V to 5.75V and -1V to -0.5V). An equation was fit to the line, and the x-intercept was calculated. The oxidation potential was found to be 4.83V.

Reduction potential was -0.15V. The SPAN cells were cycled from 1-2.7V. The GPE is stable across that range.

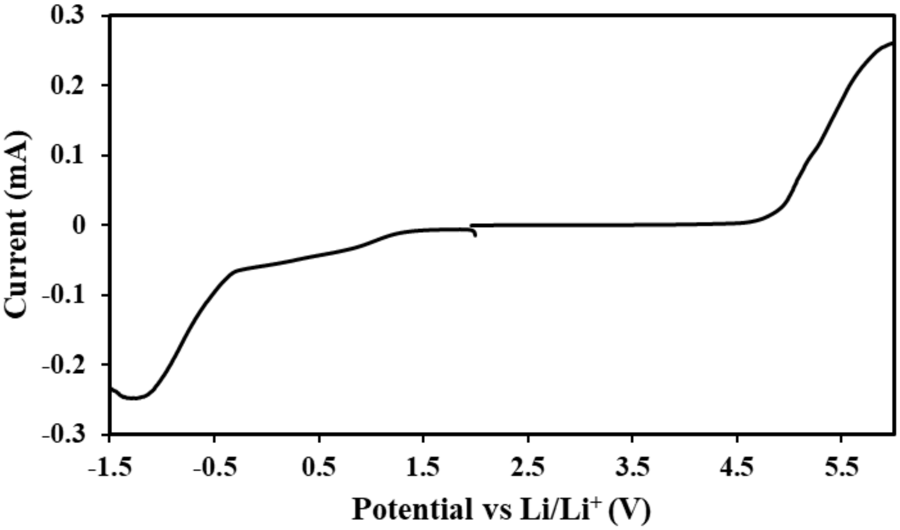

Figure 6: Linear Sweep Voltammetry of PVDF-HPE GPE with SS and Li Electrodes.

The ionic conductivity of the interlayer was found with the results of EIS of the GPE between two SS electrodes. A Nyquist plot was obtained in figure 6 below. The GPE exhibited an x-intercept and Warhburg tail without any semicircle. This is indicative of a flooded cell, where only the liquid is responsible for the conduction of charge. The bulk resistance of the GPE is the x-intercept of the graph, which was 57Ωcm^2. Equation (4) was then used to calculate the ionic conductivity. The ionic conductivity was found to be 5.12x10^{-4} Scm^{-1}, which on the same order of magnitude as LLZTO.[15]

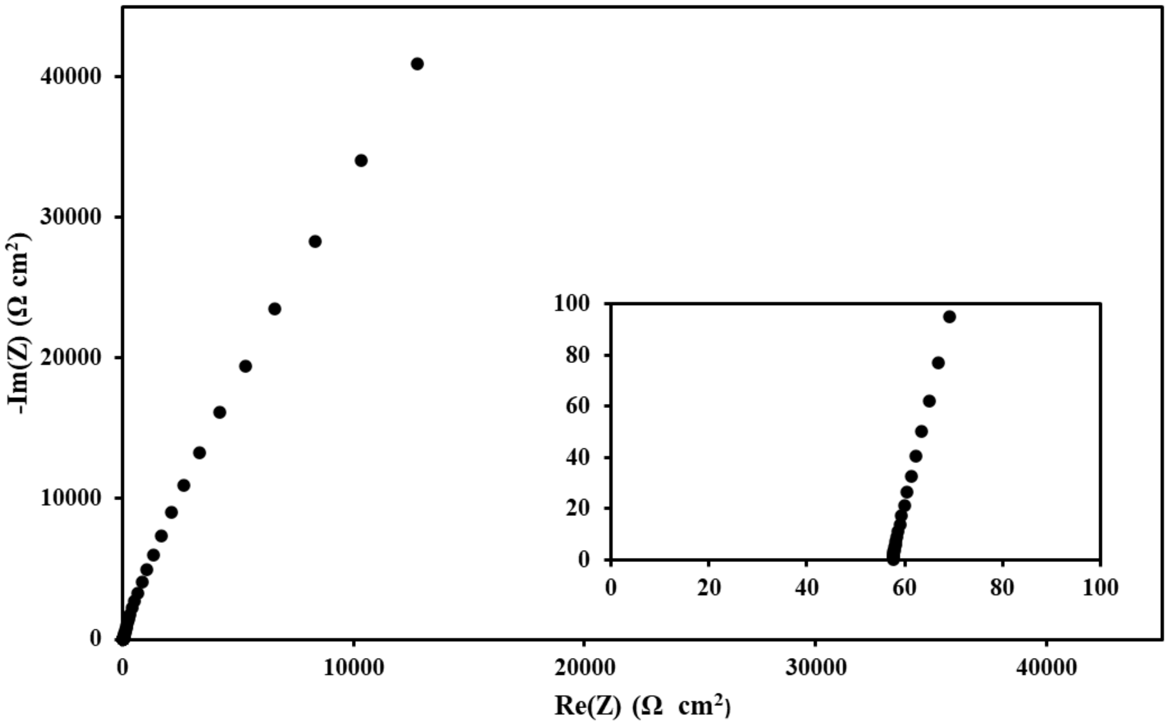

Figure 7: EIS of GPE between SS electrodes 1HZ to 1MHZ.

Lithium conductivity must be separated from the ionic conductivity using the transference number. Using the Bruce-Vincent method, the results of the impedance (figure 7) and DC polarization experiments (figure 8) are seen below. The impedance data allows us to correct for electrode effects on the polarization. We can see a large impedance increase between before the DC polarization experiment and after. The impedance could be due to SEI growth. Additionally, there are two semicircles on the graph. The first semicircle (left) represents the bulk resistance and is from the high frequency region. The second semicircle is from the low frequency region and electrode-electrolyte interfacial resistance.[34] The interfacial resistance is required for the transference number. It can be taken from the graph by subtracting the resistance from the end of the first semicircle and from the end of the second semicircle. In the DC polarization experiment, the current is oscillating. Therefore, it is difficult to find a steady state current once the line settles. So, the steady state current was estimated by averaging the current over the last 20 minutes of testing. The values were then used to calculate the transference number. The transference number was found to be 0.103. The transference number and the ionic conductivity can be used to find the lithium conductivity, which is 5.28x10^{-5} Scm^{-1}. The transference number is low which shows that the lithium cations have a much stronger interaction with the polymer chains than the TFSI anions. This makes the LLZTO a better lithium conductor than the GPE because the LLZTO is a single ion conductor, which allows the LLZTO to not be hampered by concentration gradients.

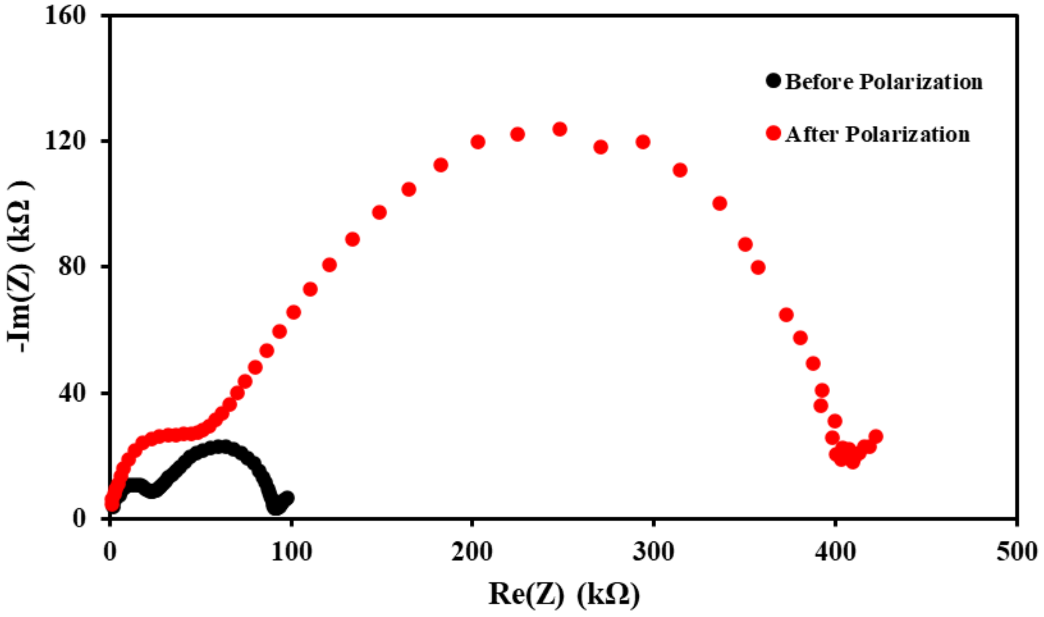

Figure 8:EIS of GPE between Li 1HZ to 1MHZ

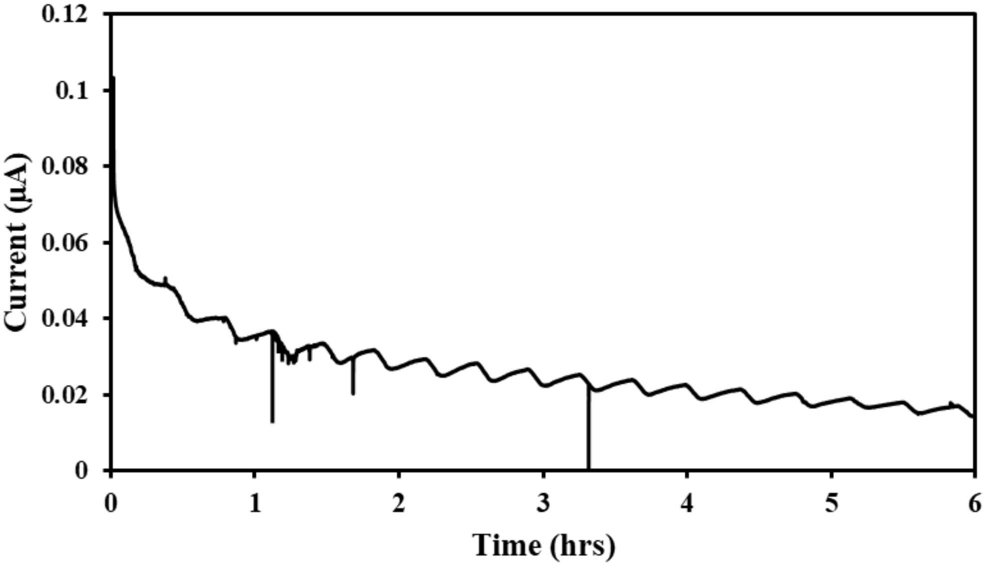

Figure 9: DC polarization 10mV potential applied over 6hrs.

4.1.2 Cycling Results

Extended cycling results were able to be obtained for three cell types. LLZTO bilayer, MIEC bilayer, and MIEC trilayers were cycled with a PVDF-HFP interlayer and SPAN cathode. LLZTO bilayer is defined as a bilayer where the porous layer and dense layer are both LLZTO. In the MIEC bilayer and trilayer, the dense layer is LLZTO and the porous layer(s) is MIEC. It is expected that having MIEC will aid lithium plating and striping. All cells were first cycled at C/4. The C/4 rate was chosen because even though SPAN has greater ionic conductivity than sulfur it is still not very kinetically fast. At higher rates, overpotentials can grow lowering the specific capacity. The graphs are reported in per g of sulfur in SPAN. Therefore, if all the sulfur was used in the SPAN the maximum capacity would be 1670mAh/g S. The reason the graphs are reported in per g of sulfur is because it allows comparison between batches of SPAN as there can be some variation of the sulfur content between batches. As well as to measure the percent sulfur utilization, which isn't as apparent in per gram active. The sulfur utilization can be found by dividing the specific capacity on the graph by 1670 mAh/g. Not shown on graphs made is the results of the formation cycle. Typical behavior of the formation cycle is that the discharge at C/20 goes well beyond the theoretical maximum discharge capacity. This could be because of reactions taking place in SPAN that are not seen during standard cell cycling.

The first cell constructed was the LLZTO bilayer. The cell's performance can be seen below in figures 10 and 11. The cell had poor performance. The initial specific capacity was 671 mAh/g S. The capacity retention was poor with the 80% capacity retention mark being 9 cycles. The average coulombic efficiency over 75 cycles was 99.5%. The average specific capacity over 775 cycles was 455 mAh/g S. The cell exhibited a sharp drop off in capacity and there is a slowdown in the rate at which the cell's capacity fades. This can be seen in figure 11 where the capacity for cycles 25,50 and 75 are much closer together than 1.

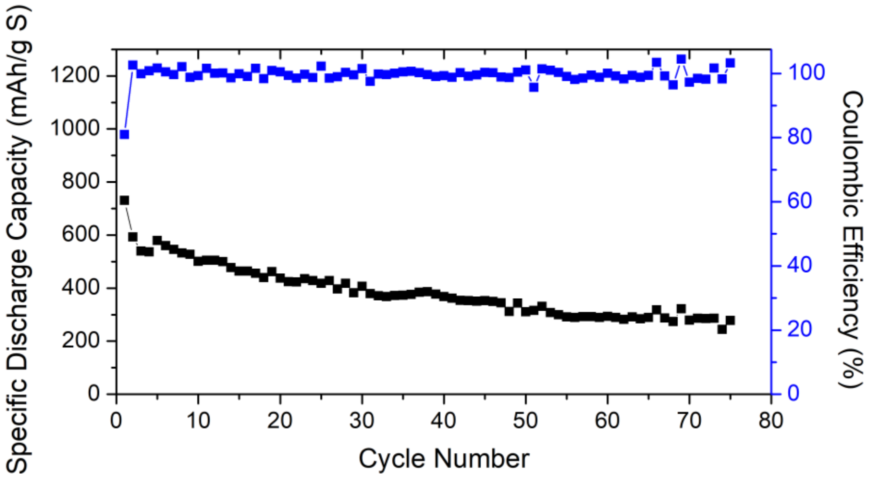

Figure 10: LLZTO bilayer with PVDF-HFP interlayer

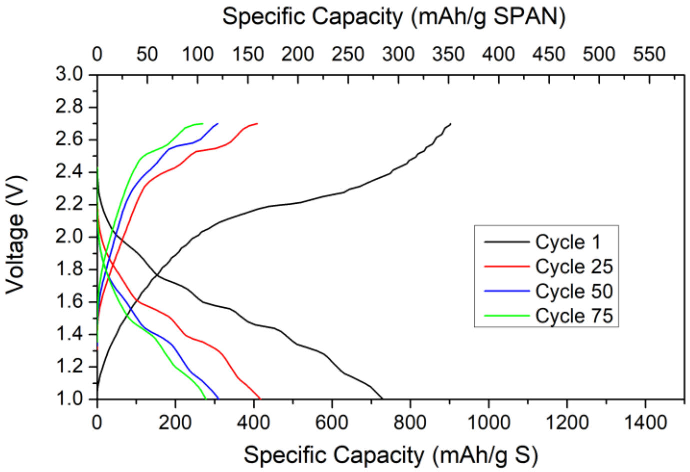

Figure 11:LLZTO bilayer with PVD-HFP interlayer

The second cell to be assembled was the MIEC bilayer. The MIEC bilayer's performance is summarized in figures 12 and 13 below. The performance was much better with the inclusion of MIEC than without. The cell's initial capacity was 824 mAh/g S. The 80% capacity retention was 303 cycles. The average coulombic efficiency over 200 cycles was 98.6%. The average specific capacity over 200 cycles was 788 mAh/g S. However, the rate at which the capacity starts to fall got faster at around cycle 300. As the cycle number increased so did the variability of the capacity. The cell seemed to have a larger overpotential when compared to the other cells. This is because the cell was hitting the CV charge cutoff earlier while the other cells reached the voltage cutoff and did not use CV charging this much. This could be due to a higher impedance of the cell. The cell went to 600 cycles. However, as can be seen in figure 13, the discharge portion of the voltage curve has become very noisy. The cell had aged too much to continue cycling.

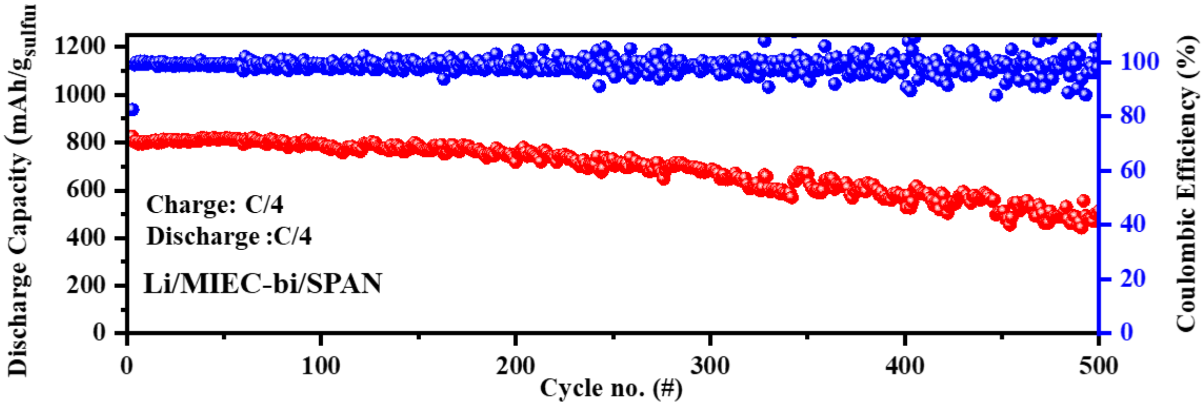

Figure 12: MIEC bilayer with PVDF-HFP interlayer

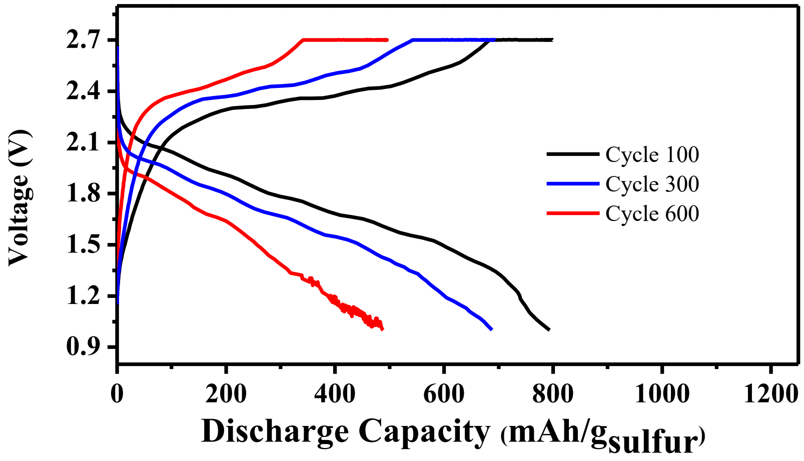

Figure 13: MIEC bilayer with PVDF-HFP interlayer.

The third and final cell constructed was the MIEC trilayer. The MIEC trilayer was cycled at C/4 for the first 200 cycles and then it was increased to 1C after the 200th cycle. The cell's performance is summarized in figures 14 and 15 below. The cell displayed very high initial capacity of 1044 mA/g. The average coulombic efficiency was 96.8% over 200 cycles. The average specific capacity was 994 mAh/g S over 200 cycles. The 80% capacity retention mark was hit at 200 cycles only because the cell's capacity dropped when increasing the rate. The rate of capacity fading was not greatly affected by the change in rate.

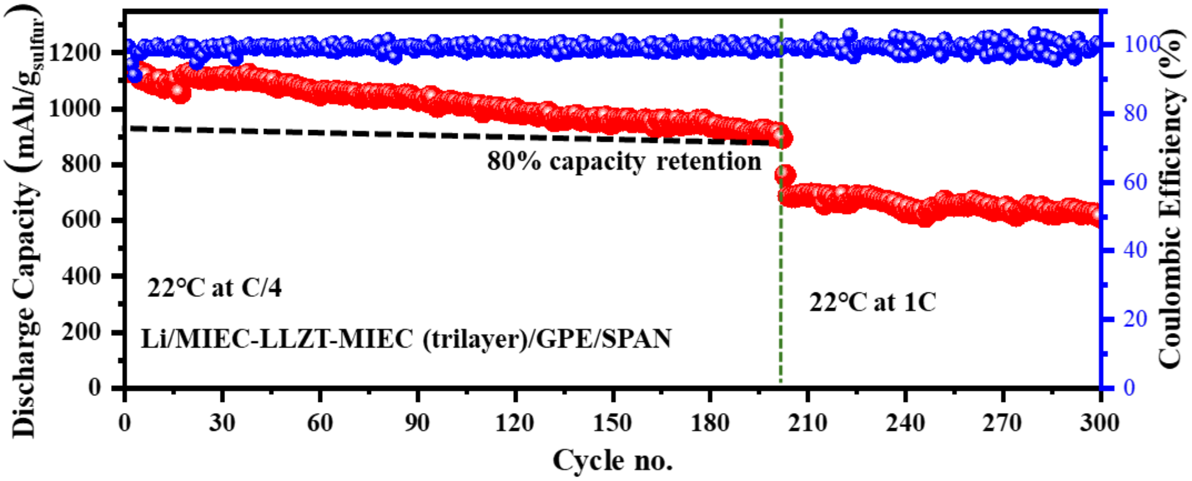

Figure 14: MIEC trilayer with PVDF-HFP interlayer

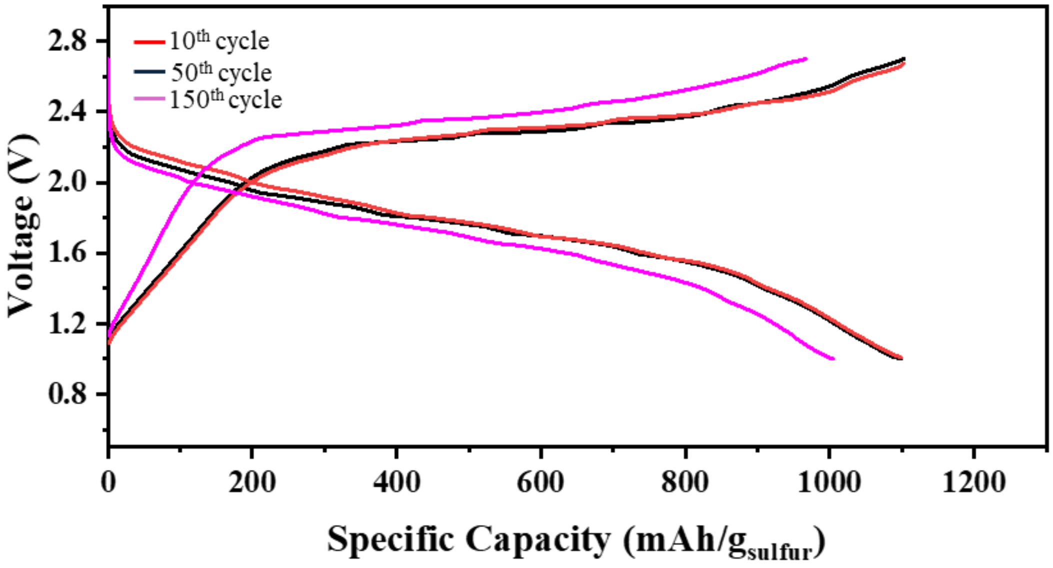

Figure 15: MIEC trilayer

The performance of the three cells made is summarized below on the same graph in figure 16. 200 cycles were chosen because all cells have data at C/4 cycling rate over that portion. The MIEC trilayer cycling rate increases after 200 cycles. Over the first 200 cycles, the MIEC trilayer performed the best. It had the highest specific capacity and retained the capacity advantage over the whole 200 cycles. It is worth noting that the rate of capacity fade appeared to be greater in the MIEC trilayer than the MIEC bilayer. The LLZTO bilayer performed the worst of all the cells. It had lower initial capacity and greater capacity fade than the other two cells.

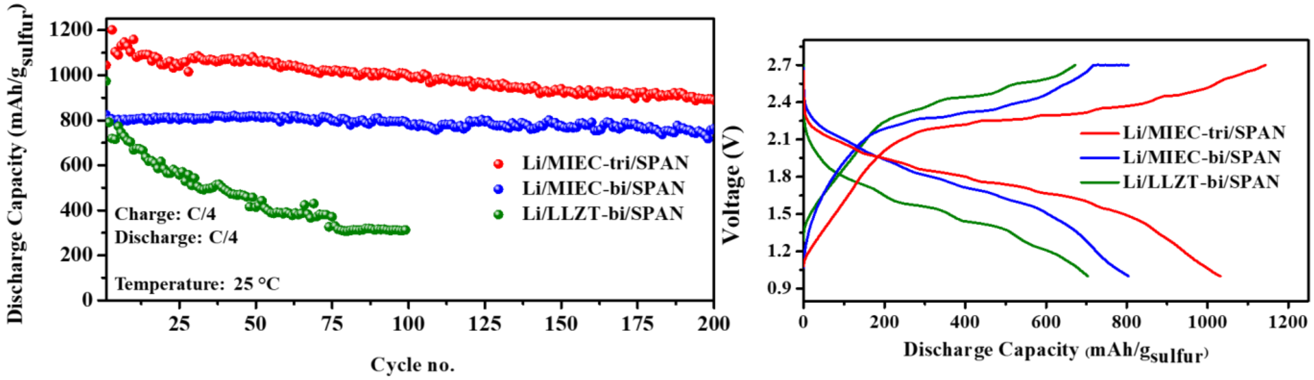

Figure 16: Selected Cycle 25. Comparison of all SPAN PVDF-HFP cells

Chapter 5: Conclusions and Recommendations

4.1 Conclusions

4.1.1 Li-SPAN Cells

MIEC structures were able to be made. However, MIEC's properties differ slightly from LLZO's. The first difference is that the tapes created with MIEC powder are tackier. This requires consideration with the sacrificial tape to prevent the tape from sticking to it. The second is that the MEIC tape is more prone to pore collapse than the LLZTO tape. To remedy pore collapse, a lower sintering temperature was chosen. However, this caused more defects in the dense tape, such as voids to be observed.

4.1.2 PVDF-HFP Interlayer

The PVDF-HFP interlayers were able to be fabricated simply, and the thickness was able to be tuned. The minimum thickness allowed was 40µm because any lower the interlayer could not be peeled off the support. The interlayer was characterized. The liquid uptake was 201%. The lithium conductivity was measured to be 5.28×10^{-5} Scm^{-1} and the transference number was 0.103. The low transference number indicates that the lithium cations have a much stronger interaction with the polymer backbone in the GPE than the TFSI anions. So, even though the ionic conductivity of the GPE close to the LLZO, the low transference number causes the lithium conductivity to be lower than the LLZO.

4.1.3 Li-SPAN cells

Three cell types were constructed and tested. The extra electronic conductivity from the MIEC improves the performance of the cells. In the MIEC bilayer and trilayer we were able to see long cycle life with the bilayer reaching 600 cycles. The capacity retention was strong with 80% capacity retention being reached in 303 cycles by the MIEC bilayer. The MIEC trilayer exhibited the best performance with the highest initial capacity as well as the highest average capacity over 200 cycles. The capacity fade appears to be lowest in the MEIC bilayer.

4.2 Recommendations

4.2.1 Recommendations

All the cells exhibited capacity loss. The use of carbonate-based electrolytes is recommended. The electrolyte in this work only uses ether-based electrolytes. While ether-based electrolytes are the standard for Li-S cells. It has been shown in SPAN cells that ethers can form soluble lithium polysulfides.[35] The generation of soluble lithium polysulfides can lead to capacity loss due to the deposition of lithium sulfide not connected to the cathode. However, SPAN is compatible with carbonate electrolytes unlike traditional sulfur cathode.[20] The use of carbonate electrolytes would prevent the formation of soluble lithium polysulfides. Therefore, the reversibility of the cathode would be improved. Furthermore, due to the solid separator protecting the anode, there are no concerns with lithium metal degradation that are usually associated with carbonate electrolytes in sulfur containing cells. It would be beneficial to examine the improvement in cell cycle life using carbonate electrolytes in these cells.

A thin interlayer is recommended. The interlayer in the cells was measured to be very thick (80μm). Due to the solid separator, there isn't needs for strong mechanical properties. Therefore, finding ways to create a thin polymer interlayer on top of the ceramic would be beneficial. However, the ceramic, once lithium infiltrated, needs to be confined to an inert atmosphere. This limits the type of methods that can be done to create interlayers. If the interlayer is too thin it might not be freestanding and would have to be formed in-situ on the ceramic. Poly-DOL was used in the past to create polymer layers on the ceramic. However, the reaction can be sluggish at varying salt concentration levels and difficult to control due to DOL's volatility.

The salt level of PVDF-HFP GPEs can be optimized. The invention of "Polymer in Salt" GPEs further aids ionic conductivity. At high level salt levels, (>50%wt.) residual solvent from the solvent casting process was found to form a salt complex within the electrolyte.[28] The complex aids lithium transport and cycling stability.[36] The development of these quasi-solid state separators could be used in garnet type solid state cells as a separator, allowing for little to no use of liquid electrolyte.

The MIEC porous layers led to the need to sinter at lower temperatures to avoid collapse of the porous layer. The lower temperatures for sintering led to more defect formation in the dense layer, lowering yield of samples. Finding a way to either prevent pore collapse at 1100°C or to further lower the sintering temperature with dopants in the LLZO could improve yield. A potential solution is the use of different dopants to the LLZO that can further lower sintering temperature. Ga is a possible dopant. A MIEC bilayer was sintered using Ga-doped and the SEM is described in appendix A.2. However, no cycling data was obtained with the bilayer.

Further study into overcharge mechanisms would be beneficial. Shi et. al. attributed overcharge to La segregation in LLZO based cells.[7] However, research in liquid cells attribute overcharge to high sulfur loading and cathode morphology creating regions of high current that lead to shorting behavior.[37] Li et. al. also attributed sulfur coating the current collector during cycling leading to overcharge.[38] A greater understanding of overcharge would allow the use of just garnet structures instead of adding a GPE to protect the garnet layer.

Appendices

Appendix A

A.1 Calculation of SPAN Sulfur Content

Table A1: Elemental analysis of Carbon and Nitrogen in SPAN sample.

ELEMENT	Weight Percent (%)
C	46
N	17

The sulfur weight percentage based on the elemental analysis is:
S(wt.%) + H(wt.%) +C(wt.%) +N(wt.%) = 100%
100%–46%–17%= 37% = S(wt.%) + H(wt.%)
Considering that hydrogen atoms make up less than 1% of the weight of SPAN and cannot be detected by the elemental analyzer. The hydrogen weight percentage can be ignored and the final weight percentage of sulfur used in the calculations of this document are 37%.

A.2 Additional SEM Images of Garnet Separators

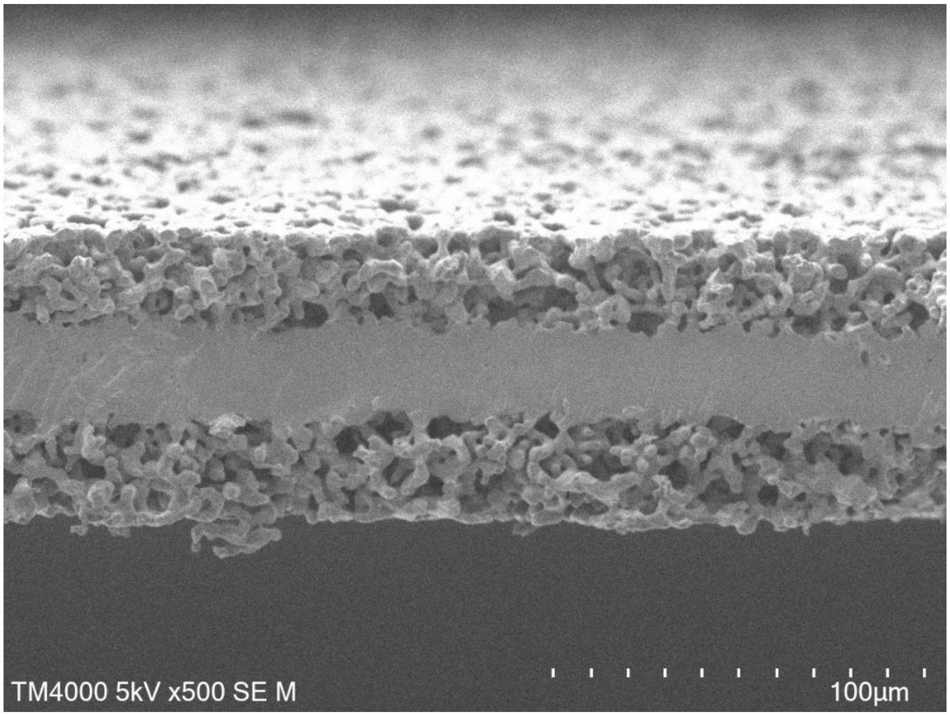

Figure A1: MIEC trilayer Sintered at 1050°C for 3hrs.

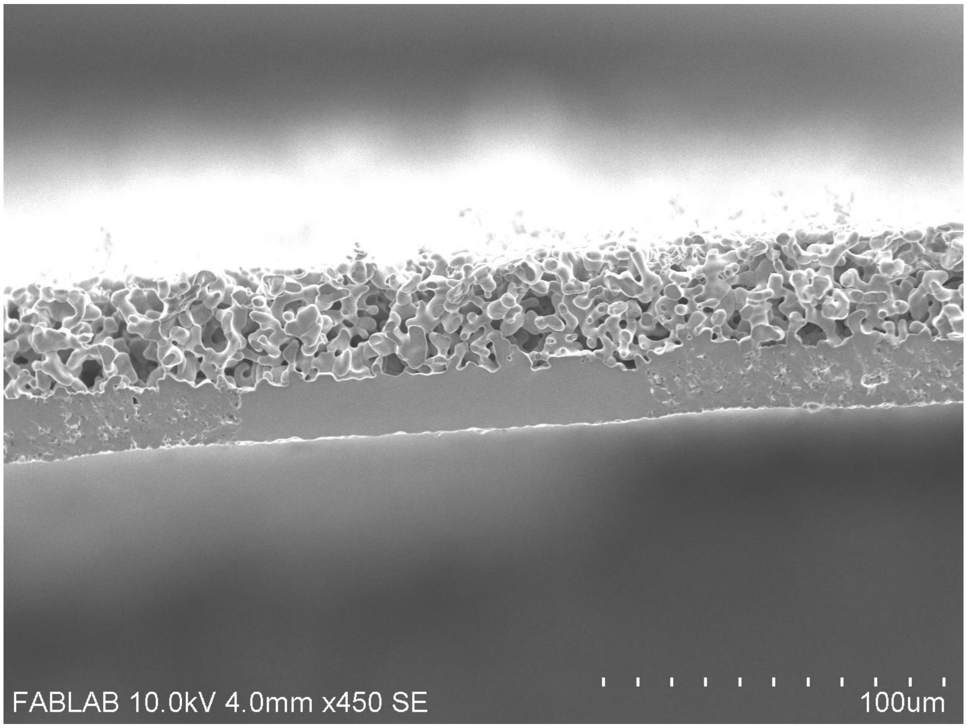

Figure A2: MIEC bilayer sintered at 1050°C for 3hrs with Ga doped LLZO

Bibliography

(1) Ritchie, H. Cars, Planes, Trains: Where Do CO_2 Emissions from Transport Come From? *Our World in Data* **2020**.

(2) Degen, F.; Winter, M.; Bendig, D.; Tübke, J. Energy Consumption of Current and Future Production of Lithium-Ion and Post Lithium-Ion Battery Cells. *Nat Energy* **2023**, *8* (11), 1284–1295. https://doi.org/10.1038/s41560-023-01355-z.

(3) Xu, W.; Wang, J.; Ding, F.; Chen, X.; Nasybulin, E.; Zhang, Y.; Zhang, J.-G. Lithium Metal Anodes for Rechargeable Batteries. *Energy Environ. Sci.* **2014**, *7* (2), 513–537. https://doi.org/10.1039/C3EE40795K.

(4) Wang, C.; Fu, K.; Kammampata, S. P.; McOwen, D. W.; Samson, A. J.; Zhang, L.; Hitz, G. T.; Nolan, A. M.; Wachsman, E. D.; Mo, Y.; Thangadurai, V.; Hu, L. Garnet-Type Solid-State Electrolytes: Materials, Interfaces, and Batteries. *Chem. Rev.* **2020**, *120* (10), 4257–4300. https://doi.org/10.1021/acs.chemrev.9b00427.

(5) Alexander, G. V.; Shi, C.; O'Neill, J.; Wachsman, E. D. Extreme Lithium-Metal Cycling Enabled by a Mixed Ion- and Electron-Conducting Garnet Three-Dimensional Architecture. *Nat. Mater.* **2023**, *22* (9), 1136–1143. https://doi.org/10.1038/s41563-023-01627-9.

(6) Zhu, L.; Zhang, X.; Zhang, J.; Ren, H.; Yao, Y.; Wang, M.; Song, Y. A Review on Sulfur-Based Composite Cathode Materials for Lithium-Sulfur Batteries: Progress and Prospects. *Journal of Alloys and Compounds* **2025**, *1010*, 178282. https://doi.org/10.1016/j.jallcom.2024.178282.

(7) Shi, C.; Hamann, T.; Takeuchi, S.; Alexander, G. V.; Nolan, A. M.; Limpert, M.; Fu, Z.; O'Neill, J.; Godbey, G.; Dura, J. A.; Wachsman, E. D. 3D Asymmetric Bilayer Garnet-Hybridized High-Energy-Density Lithium–Sulfur Batteries. *ACS Appl. Mater. Interfaces* **2023**, *15* (1), 751–760. https://doi.org/10.1021/acsami.2c14087.

(8) Alarco, J.; Talbot, P.; Conversation, T. *The history and development of batteries*. https://phys.org/news/2015-04-history-batteries.html (accessed 2025-10-31).

(9) *Nobel Prize in Chemistry 2019*. NobelPrize.org. https://www.nobelprize.org/prizes/chemistry/2019/summary/ (accessed 2025-10-31).

(10) Asenbauer, J.; Eisenmann, T.; Kuenzel, M.; Kazzazi, A.; Chen, Z.; Bresser, D. The Success Story of Graphite as a Lithium-Ion Anode Material – Fundamentals, Remaining Challenges, and Recent Developments Including Silicon (Oxide) Composites. *Sustainable Energy & Fuels* **2020**, *4* (11), 5387–5416. https://doi.org/10.1039/D0SE00175A.

(11) Monroe, C.; Newman, J. The Impact of Elastic Deformation on Deposition Kinetics at Lithium/Polymer Interfaces. *J. Electrochem. Soc.* **2005**, *152* (2), A396. https://doi.org/10.1149/1.1850854.

(12) Bachman, J. C.; Muy, S.; Grimaud, A.; Chang, H.-H.; Pour, N.; Lux, S. F.; Paschos, O.; Maglia, F.; Lupart, S.; Lamp, P.; Giordano, L.; Shao-Horn, Y. Inorganic Solid-State Electrolytes for Lithium Batteries: Mechanisms and Properties Governing Ion Conduction. *Chem. Rev.* **2016**, *116* (1), 140–162. https://doi.org/10.1021/acs.chemrev.5b00563.

(13) Murugan, R.; Thangadurai, V.; Weppner, W. Fast Lithium Ion Conduction in Garnet-Type $Li_7 La_3 Zr_2 O_{12}$. *Angew Chem Int Ed* **2007**, *46* (41), 7778–7781. https://doi.org/10.1002/anie.200701144.

(14) Geiger, C. A.; Alekseev, E.; Lazic, B.; Fisch, M.; Armbruster, T.; Langner, R.; Fechtelkord, M.; Kim, N.; Pettke, T.; Weppner, W. Crystal Chemistry and Stability of

"Li7La3Zr2O12" Garnet: A Fast Lithium-Ion Conductor. *Inorg. Chem.* **2011**, *50* (3), 1089–1097. https://doi.org/10.1021/ic101914e.

(15) Wang, Y.; Lai, W. High Ionic Conductivity Lithium Garnet Oxides of Li7−xLa3Zr2−xTaxO12 Compositions. *Electrochem. Solid-State Lett.* **2012**, *15* (5), A68. https://doi.org/10.1149/2.024205esl.

(16) Ye, Y.; Song, M.-K.; Xu, Y.; Nie, K.; Liu, Y.; Feng, J.; Sun, X.; Cairns, E. J.; Zhang, Y.; Guo, J. Lithium Nitrate: A Double-Edged Sword in the Rechargeable Lithium-Sulfur Cell. *Energy Storage Materials* **2019**, *16*, 498–504. https://doi.org/10.1016/j.ensm.2018.09.022.

(17) Wang, J.; Yang, J.; Xie, J.; Xu, N. A Novel Conductive Polymer–Sulfur Composite Cathode Material for Rechargeable Lithium Batteries. *Advanced Materials* **2002**, *14* (13–14), 963–965. https://doi.org/10.1002/1521-4095(20020705)14:13/14%253C963::AID-ADMA963%253E3.0.CO;2-P.

(18) Phan, A. L.; Le, P. M. L.; Wang, C. Realizing High-Energy and Long-Life Li/SPAN Batteries. *Joule* **2024**, *8* (6), 1601–1618. https://doi.org/10.1016/j.joule.2024.04.003.

(19) Ahmed, M. S.; Lee, S.; Agostini, M.; Jeong, M.-G.; Jung, H.-G.; Ming, J.; Sun, Y.-K.; Kim, J.; Hwang, J.-Y. Multiscale Understanding of Covalently Fixed Sulfur–Polyacrylonitrile Composite as Advanced Cathode for Metal–Sulfur Batteries. *Advanced Science* **2021**, *8* (21), 2101123. https://doi.org/10.1002/advs.202101123.

(20) Miao, Q.; Solan, N.; Hyun, G.; Holoubek, J.; Liu, P. Electrolyte Engineering for Long-Life Li-SPAN Batteries. *ACS Energy Lett.* **2023**, *8* (11), 4818–4830. https://doi.org/10.1021/acsenergylett.3c01711.

(21) Zhang, Y.; Wang, S.; Li, C.; Wang, Z.; Ma, Y.; Shi, X.; Zhang, H.; Song, D.; Zhang, L. Pvdf. *EcoEnergy* **2025**, *3* (1), 56–76. https://doi.org/10.1002/ece2.74.

(22) Ahmed, Md. S.; Islam, M.; Raut, B.; Yun, S.; Kim, H. Y.; Nam, K.-W. A Comprehensive Review of Functional Gel Polymer Electrolytes and Applications in Lithium-Ion Battery. *Gels* **2024**, *10* (9), 563. https://doi.org/10.3390/gels10090563.

(23) Aruchamy, K.; Ramasundaram, S.; Divya, S.; Chandran, M.; Yun, K.; Oh, T. H. Gel Polymer Electrolytes: Advancing Solid-State Batteries for High-Performance Applications. *Gels* **2023**, *9* (7), 585. https://doi.org/10.3390/gels9070585.

(24) Hitz, G. T.; McOwen, D. W.; Zhang, L.; Ma, Z.; Fu, Z.; Wen, Y.; Gong, Y.; Dai, J.; Hamann, T. R.; Hu, L.; Wachsman, E. D. High-Rate Lithium Cycling in a Scalable Trilayer Li-Garnet-Electrolyte Architecture. *Materials Today* **2019**, *22*, 50–57. https://doi.org/10.1016/j.mattod.2018.04.004.

(25) Han, X.; Gong, Y.; Fu, K. (Kelvin); He, X.; Hitz, G. T.; Dai, J.; Pearse, A.; Liu, B.; Wang, H.; Rubloff, G.; Mo, Y.; Thangadurai, V.; Wachsman, E. D.; Hu, L. Negating Interfacial Impedance in Garnet-Based Solid-State Li Metal Batteries. *Nature Mater* **2017**, *16* (5), 572–579. https://doi.org/10.1038/nmat4821.

(26) Fu, K. "Kelvin"; Gong, Y.; Xu, S.; Zhu, Y.; Li, Y.; Dai, J.; Wang, C.; Liu, B.; Pastel, G.; Xie, H.; Yao, Y.; Mo, Y.; Wachsman, E.; Hu, L. Stabilizing the Garnet Solid-Electrolyte/Polysulfide Interface in Li–S Batteries. *Chem. Mater.* **2017**, *29* (19), 8037–8041. https://doi.org/10.1021/acs.chemmater.7b02339.

(27) Shi, C.; Takeuchi, S.; Alexander, G. V.; Hamann, T.; O'Neill, J.; Dura, J. A.; Wachsman, E. D. High Sulfur Loading and Capacity Retention in Bilayer Garnet Sulfurized-Polyacrylonitrile/Lithium-Metal Batteries with Gel Polymer Electrolytes. *Advanced Energy Materials* **2023**, *13* (42), 2301656. https://doi.org/10.1002/aenm.202301656.

(28) Carena, E.; Mezzomo, L.; Vallana, N.; Ceribelli, N.; Di Liberto, G.; Mostoni, S.; Ferrara, C.; Mauri, M.; Lorenzi, R.; Giordano, L.; Ruffo, R.; Mustarelli, P. PVDF-HFP Based, Quasi-Solid Nanocomposite Electrolytes for Lithium Metal Batteries. *Small* **2024**, *20* (30), 2311805. https://doi.org/10.1002/smll.202311805.

(29) *Basics of EIS: Electrochemical Research-Impedance Gamry Instruments*. https://www.gamry.com/application-notes/EIS/basics-of-electrochemical-impedance-spectroscopy/ (accessed 2025-11-14).

(30) Bruce, P. G.; Evans, J.; Vincent, C. A. Conductivity and Transference Number Measurements on Polymer Electrolytes. *Solid State Ionics* **1988**, *28–30*, 918–922. https://doi.org/10.1016/0167-2738(88)90304-9.

(31) *How to read battery cycling curves - BioLogic Learning Center*. BioLogic. https://www.biologic.net/topics/how-to-read-cycling-curves/ (accessed 2025-11-18).

(32) Nanakoudis, A. *What is scanning electron microscopy?*. Advancing Materials. https://www.thermofisher.com/blog/materials/what-is-sem-scanning-electron-microscopy-explained/ (accessed 2025-11-18).

(33) Han, F.; Westover, A. S.; Yue, J.; Fan, X.; Wang, F.; Chi, M.; Leonard, D. N.; Dudney, N. J.; Wang, H.; Wang, C. High Electronic Conductivity as the Origin of Lithium Dendrite Formation within Solid Electrolytes. *Nat Energy* **2019**, *4* (3), 187–196. https://doi.org/10.1038/s41560-018-0312-z.

(34) Ravi, M.; Song, S.; Wang, J.; Wang, T.; Nadimicherla, R. Ionic Liquid Incorporated Biodegradable Gel Polymer Electrolyte for Lithium Ion Battery Applications. *J Mater Sci: Mater Electron* **2016**, *27* (2), 1370–1377. https://doi.org/10.1007/s10854-015-3899-x.

(35) Zhang, S. S. Understanding of Sulfurized Polyacrylonitrile for Superior Performance Lithium/Sulfur Battery. *Energies* **2014**, *7* (7), 4588–4600. https://doi.org/10.3390/en7074588.

(36) Zhang, J.; Zeng, Y.; Li, Q.; Tang, Z.; Sun, D.; Huang, D.; Zhao, L.; Tang, Y.; Wang, H. Polymer-in-Salt Electrolyte Enables Ultrahigh Ionic Conductivity for Advanced Solid-State Lithium Metal Batteries. *Energy Storage Materials* **2023**, *54*, 440–449. https://doi.org/10.1016/j.ensm.2022.10.055.

(37) *Insights into the Overcharge-Induced Failure Mechanism of Lithium–Sulfur Batteries - Deng - Batteries & Supercaps - Wiley Online Library*. https://chemistry-europe.onlinelibrary.wiley.com/doi/full/10.1002/batt.202500350?casa_token=8mtCoSw1FFMAAAAA%3A1UMnv8FaEsPuUIM4Zx0q-kkZBd0avdt_kc9DKZZqHUDPPVFqTLFeRjgBwqpI8Q0WbkOVAc0zN_lGMZjH (accessed 2025-11-13).

(38) Li, R.; Zeng, Y.; Song, L.; Lv, J.; Wang, C.; Zhou, C.; Cai, S.; Chen, T.; Yue, S.; Ma, K.; Yue, H. Mechanism and Solution of Overcharge Effect in Lithium–Sulfur Batteries. *Small* **2024**, *20* (2), 2305283. https://doi.org/10.1002/smll.202305283.